



Lagrangian Stochastic Modeling of Unstable Atmospheric Surface Layer

Jihoon Shin¹ · Jong-Jin Baik²

Received: 9 September 2024 / Accepted: 30 December 2024
© The Author(s) 2025

Abstract

This study evaluates the performance of a recently developed Lagrangian stochastic model (LSM), which solves the transport equations for turbulence probability density functions (PDFs), for simulating the unstable atmospheric surface layer (ASL). The simulated statistics are compared with the Monin-Obukhov similarity theory (MOST) predictions for mean gradients, standard deviations, turbulent Prandtl number, turbulence kinetic energy budgets, and turbulence PDFs. The LSM successfully captures many aspects of ASL structure and turbulence characteristics, particularly the mean gradients and standard deviations of potential temperature, specific humidity, and vertical velocity, which align closely with MOST predictions. However, the model shows limitations in reproducing the stability dependency of mean gradients of horizontal wind speed. Additionally, the model underestimates the probability of high vertical velocity fluctuations, leading to underprediction of turbulent transport and thermal convection initiation. The simulated turbulent Prandtl number shows dependency on stability but is generally weaker than MOST predictions. The study identifies that the parameterizations of dissipation, pressure redistribution, and pressure transport need to be enhanced to ensure that they have correct stability dependency, in order to improve the model's accuracy in simulating the ASL.

Keywords Atmospheric surface layer · Lagrangian stochastic modeling · Monin–Obukhov similarity theory

1 Introduction

The atmospheric surface layer (ASL) constitutes the lowest part of the atmospheric boundary layer, where proximity to the surface limits the scale of turbulence. The accurate modeling of ASL is crucial for numerical atmospheric models, as this layer determines the exchanges of momentum, heat, and moisture between the surface and the atmosphere. However, the characteristics of turbulence within the ASL are significantly modulated by the surface, so

✉ Jihoon Shin

✉ Jong-Jin Baik
jjbaik@snu.ac.kr

¹ Department of Environmental Atmospheric Sciences, Pukyong National University, Busan, South Korea

² School of Earth and Environmental Sciences, Seoul National University, Seoul, South Korea

the traditional turbulence modeling methods fall short of simulating ASL. The structure of turbulence and mean vertical profiles in ASL is typically modeled using the Monin–Obukhov similarity theory (MOST) (Monin and Obukhov 1954). MOST provides empirically determined universal functions for mean wind profiles (Businger et al. 1971; Dyer 1974; Högström 1988), standard deviations (Andreas et al. 1998; Liu et al. 1998; Wilson 2008), and turbulence kinetic energy budgets (Högström 1990; McNaughton 2006) as functions of a dimensionless stability parameter. Despite deficiencies in MOST, like neglecting the non-local turbulence effect and surface heterogeneity, the near-surface behavior of the turbulence model is expected to be consistent with MOST for moderately unstable or stable ASL.

Consistent modeling of ASL and the upper portions of the atmospheric boundary layer has historically posed significant challenges in atmospheric turbulence modeling. Atmospheric turbulence models are often not fully consistent with MOST and produce profiles that deviate from those predicted by MOST (van der Laan et al. 2017; Želi et al. 2019). Eddy viscosity (or first-order) turbulence models can produce wind and temperature profiles consistent with MOST when eddy viscosity is expressed using MOST stability functions (Stull 1988). However, parameterizing eddy viscosity valid for the entire boundary layer while maintaining the consistency remains complex. This issue becomes even more complicated with higher-order closure turbulence models. The atmospheric modeling community is transitioning from first-order closure models to higher-order closure or PDF-based turbulence models to achieve a more detailed representation of turbulence fluxes and realistically simulate various types of boundary layer clouds (Golaz et al. 2002; Bogenschütz et al. 2013). Despite large efforts, the near-surface behavior of uncertain terms in the second moment transport equations remains not fully understood.

Development of the MOST-consistent turbulence models has primarily focused on the k – ϵ models. Apsley and Castro (1997) introduced a limited-length-scale k – ϵ model to impose surface-layer scaling on the ϵ equation, and the model was revised by Sumner and Masson (2012) to achieve better consistency with MOST. Alinot and Masson (2005) and van der Laan et al. (2017) proposed MOST-consistent k – ϵ models by modifying the coefficient associated with the buoyancy production of dissipation. Recently, Zeng and Wang (2020) developed a MOST-consistent k – ϵ model for the convective boundary layer by including the buoyancy-induced increase in the kinetic energy. These studies have demonstrated that the MOST profiles can be reproduced by modifying coefficients or adding terms to the equations. However, because k – ϵ models typically neglect turbulence anisotropy and rely on simplified turbulent transport parameterization, these modifications are not guaranteed to be physically accurate.

The modeling of the unstable ASL is especially complicated due to the inhomogeneous and anisotropic nature of turbulence, along with the presence of thermal convection. The contribution of turbulent transport is significant within the unstable ASL (Högström 1990), but the accurate prediction of turbulent transport is difficult due to the closure problem in turbulence modeling. Existing parameterizations for turbulent transport have not been thoroughly validated for ASL modeling. If the joint probability density function (PDF) of velocity and temperature in the ASL is known, the exact turbulent transport can be calculated. Furthermore, the joint PDF can be utilized to simulate a realistic ensemble of convective updrafts in convection parameterizations. Recently developed convection parameterizations determine the initial properties of convective updrafts using joint PDF of turbulence near the surface (Suselj et al. 2019; Shin and Park 2020). Investigating joint PDFs in the ASL could also help understand various physical processes within the ASL.

In efforts to simulate the turbulence PDF in the atmospheric boundary layer, Shin and Baik (2024) explored the Lagrangian PDF method for atmospheric boundary layer modeling. This

study introduced a single-column model that explicitly solves the transport equations of turbulence PDF using a Lagrangian stochastic modeling approach. Turbulent transport is treated exactly and any turbulence statistics can be obtained in this model. The model builds on and extends previously developed stochastic differential equations (SDEs) for particle velocity and temperature (Das and Durbin 2005), allowing for the simulation of inhomogeneous turbulence. The proposed Lagrangian stochastic model (LSM) has demonstrated its capability to reasonably reproduce the PDF and statistics of inhomogeneous stratified turbulence simulated by large-eddy simulation (LES) models.

In the present study, we aim to evaluate the LSM developed by Shin and Baik (2024) for simulating the unstable ASL. Using the Lagrangian stochastic modeling framework, the impact of uncertain terms in the Reynolds stress equations can be evaluated in the context of turbulence PDF. We focus on the unstable ASL rather than the stable ASL to investigate the non-Gaussian turbulence PDF and its impact on the simulation of the ASL. To test the accuracy of the LSM simulations, we compare the simulated profiles of gradients and standard deviations of wind speed and temperature against the predictions made by MOST. By validating the LSM simulations against MOST, we aim to demonstrate that the LSM approach not only captures the complex turbulent structures within the ASL but also adheres to the well-established empirical laws governing this region. The analysis is extended to turbulence energy budget and PDFs of velocity and temperature. We also discuss how the PDF-based turbulence models can be improved to be more consistent with MOST, based on the recent theories on the ASL.

2 Theory and Method

2.1 Monin–Obukhov Similarity Theory (MOST)

MOST assumes that vertical turbulent fluxes are approximately constant with height in the ASL in the condition that the surface is homogeneous and mean flow is in a steady state. The central concept of MOST is that turbulence in the ASL is governed by universal functions that depend on the dimensionless stability parameter, defined by the ratio of height to the Obukhov length, z/L . The Obukhov length L is defined as:

$$L = -\frac{\overline{\theta}_v u_*^3}{\kappa g \left(\overline{w'\theta'_v} \right)_s}, \quad (1)$$

where the overbar and prime denote the mean and perturbation components by Reynolds averaging, respectively, $\kappa = 0.4$ is the von Kármán constant, g is the gravitational acceleration, u_* is the friction velocity, and $\overline{\theta}_v$ and $\left(\overline{w'\theta'_v} \right)_s$ is the mean virtual potential temperature and virtual potential temperature flux at the near-surface, respectively.

The dimensionless vertical gradients of potential temperature θ , specific humidity q , and horizontal wind speed u_h are given by the following similarity relationships:

$$\frac{\partial \theta}{\partial z} \frac{\kappa z}{\theta_*} = \Phi_\theta \left(\frac{z}{L} \right), \quad (2)$$

$$\frac{\partial q}{\partial z} \frac{\kappa z}{q_*} = \Phi_q \left(\frac{z}{L} \right), \quad (3)$$

$$\frac{\partial u_h}{\partial z} \frac{\kappa z}{u_*} = \Phi_m \left(\frac{z}{L} \right), \quad (4)$$

where $\theta_* = -(\overline{w'\theta'})_s/u_*$ and $q_* = -(\overline{w'q'})_s/u_*$ are the characteristic scales for potential temperature and specific humidity, respectively, $\Phi_h(\frac{z}{L})$, $\Phi_q(\frac{z}{L})$, and $\Phi_m(\frac{z}{L})$ are the dimensionless stability functions for heat, moisture, and momentum, respectively.

In addition to the mean profiles, MOST also predicts the standard deviations of potential temperature, specific humidity, and vertical velocity fluctuations in the ASL. These standard deviations are also functions of the stability parameter z/L , and are given by the following relationships:

$$\frac{\sigma_\theta}{\theta_*} = \Phi_{\sigma_\theta}\left(\frac{z}{L}\right), \quad (5)$$

$$\frac{\sigma_q}{q_*} = \Phi_{\sigma_q}\left(\frac{z}{L}\right), \quad (6)$$

$$\frac{\sigma_w}{u_*} = \Phi_{\sigma_w}\left(\frac{z}{L}\right), \quad (7)$$

where σ_θ , σ_q , and σ_w are the standard deviations of potential temperature, specific humidity, and vertical velocity, respectively, and Φ_{σ_θ} , Φ_{σ_q} , and Φ_{σ_w} are the corresponding dimensionless functions that depend on the stability of the surface layer. The dimensionless functions for vertical gradients and standard deviations are typically given in the form (the Businger-Dyer form) of:

$$\Phi = A_1(1 - A_2\frac{z}{L})^{A_3}, \quad (8)$$

where coefficients A_1 , A_2 , and A_3 have been empirically determined by many field observations.

2.2 Lagrangian Stochastic Model (LSM)

The LSM proposed by Shin and Baik (2024) is based on the PDF methods developed in 1990s for engineering purposes (Pope 1995; Van Slooten et al. 1998; Jenny et al. 2001; Muradoglu et al. 2001). In this model, a number of particles evolve by SDEs that describe the Lagrangian evolution of particle velocity and scalar properties in turbulent flow. Any turbulence statistics can then be calculated by averaging the particle properties, using a Monte Carlo approach. The SDEs for particle velocity and temperature used in the model are adopted from Das and Durbin (2005) with the inclusion of a pressure transport parameterization. The model also includes the SDE for dissipation rate adopted from Van Slooten et al. (1998), where the source of dissipation is the same as the standard k - ϵ model. In this study, the SDE for temperature is extended to any passive scalar ϕ to include the specific humidity of water vapor as a prognostic variable. The passive scalars predicted in this study are $\phi = \{\theta, q\}$ where θ is the potential temperature and q is the specific humidity of water vapor.

The equations for the particle position x_i , velocity component u_i , and passive scalar ϕ are:

$$dx_i = u_i dt, \quad (9)$$

$$\begin{aligned} du_i = & -\frac{c_1 \epsilon}{2k} u'_i dt + c_{2\phi} u'_k \frac{\partial \overline{u_i}}{\partial x_k} dt + c_{3\phi} u'_k \frac{\partial \overline{u_k}}{\partial x_i} dt \\ & - (1 - c_{5\phi}) g_i \frac{\theta'_v}{\theta_{v0}} dt + \underbrace{C_{pt} \left(\frac{u'_k u'_k}{2k} - 1 \right) \frac{\partial k}{\partial x_i} dt}_{\text{pressure transport}} + \sqrt{c_0 \epsilon} dW_i, \end{aligned} \quad (10)$$

Table 1 Model constants

Constant	Value	Constant	Value
c_1	1.8	$c_{1\phi}$	2.5
c_2	0.6	$c_{2\phi}$	0.6
c_3	0.0	$c_{3\phi}$	0.0
c_5	1/3	$c_{4\phi}$	0.0
\mathcal{R}	1.5	$c_{5\phi}$	1/3
$C_{\epsilon 1}$	1.21	C_3	1.0
$C_{\epsilon 2}$	1.92	C_4	0.25
$C_{\epsilon 3}$	0.0	C_{pt}	0.2

$$d\phi = -\left(c_{1\phi} - \frac{c_1}{2}\right) \frac{\epsilon}{k} \phi' dt + c_{4\phi} u'_k \frac{\partial \bar{\phi}}{\partial x_k} dt + \sqrt{c_\phi} dW_\phi, \quad (11)$$

where θ_v and θ_{v0} are the virtual potential temperature and basic state virtual potential temperature respectively, g_i is the component of gravitational acceleration, dW is the increment of the Wiener process, $k = (1/2)u_k'^2$ is the turbulent kinetic energy (TKE), and ϵ is the Reynolds-averaged dissipation rate. The coefficients c_0 and c_ϕ are specified as:

$$c_0 = \frac{2}{3} \left[c_1 - 1 + (c_2 + c_3) \frac{\mathcal{P}}{\epsilon} + c_5 \frac{\mathcal{G}}{\epsilon} \right], \quad (12)$$

$$c_\phi = -2c_{4\phi} \overline{u'_k \phi'} \frac{\partial \bar{\phi}}{\partial x_k} + \frac{\epsilon}{k} (2c_{1\phi} - c_1 - \mathcal{R}) \bar{\phi'^2},$$

where \mathcal{P} and \mathcal{G} are the shear production and buoyancy production, respectively. c_0 and c_ϕ are constrained to be non-negative, as suggested by Das and Durbin (2005).

The SDE for the dissipation rate is expressed in terms of turbulence frequency $\omega = \epsilon^*/k$, where ϵ^* is the local dissipation rate:

$$d\omega = -C_3(\omega - \bar{\omega})\Omega dt - \Omega \omega S_\omega dt + \sqrt{2C_3 C_4 \bar{\omega} \Omega \omega} dW, \quad (13)$$

$$S_\omega = (C_{\epsilon 2} - 1) - (C_{\epsilon 1} - 1) \frac{\mathcal{P}}{\epsilon} - (C_{\epsilon 3} - 1) \frac{\mathcal{G}}{\epsilon},$$

where $\Omega \equiv C_\Omega \langle \omega \mid \omega \geq \bar{\omega} \rangle$ ($C_\Omega \approx 0.6893$) is the conditional-mean turbulence frequency. The Reynolds-averaged dissipation is determined as $\epsilon = \Omega k$. The model constants used in this study are listed in Table 1. The value of the model constants are the same as Shin and Baik (2024), except $C_{\epsilon 1}$ is changed from 1.44 to 1.21 and $C_{\epsilon 2}$ is changed from 1.82 to 1.92. The modified $C_{\epsilon 1}$ and $C_{\epsilon 2}$ values are known to be more appropriate for atmospheric flows (Sørensen 1995) and thus used in several studies that simulate the ASL using k - ϵ models (van der Laan et al. 2017; Sørensen 1995). The value of $C_{\epsilon 3}$ is set to zero, as there is no consensus on the value of $C_{\epsilon 3}$. Alinot and Masson (2005) showed that the value of $C_{\epsilon 3}$ should be highly dependent on the stability parameter in order for the k - ϵ model to simulate correct MOST profiles.

The numerical implementation of the model can be summarized as follows. At each time step, the particle properties and positions are advanced using a second-order time integration scheme. Proper boundary conditions and surface fluxes are imposed on the particles. A vertical grid is defined and turbulence statistics are calculated by averaging the particle values at each vertical layer. From the calculated turbulent fluxes, the evolution of mean

Table 2 List of Symbols

Symbol	Description
u, v, w	Velocity components in the x , y , and z directions, respectively
θ, θ_v, q	Potential temperature, virtual potential temperature, and specific humidity
L	Obukhov length
κ	von Kármán constant
g	Gravitational acceleration
u_*	Friction velocity
θ_*, q_*	Characteristic scales for θ and q , respectively
Φ_h, Φ_q, Φ_m	Dimensionless similarity functions for heat, moisture, and momentum, respectively
$\sigma_\theta, \sigma_q, \sigma_w$	Standard deviations of θ , q , and w , respectively
$\Phi_{\sigma_\theta}, \Phi_{\sigma_q}, \Phi_{\sigma_w}$	Dimensionless similarity functions for σ_θ , σ_q , and σ_w , respectively
ϕ	Passive scalar, such as θ or q
k	Turbulent kinetic energy (TKE)
$\mathcal{P}, \mathcal{G}, T^t, T^p, \epsilon$	Shear production, buoyancy production, turbulent transport, pressure transport, and dissipation of TKE, respectively
ω	Turbulence frequency
Ω	Conditional-mean turbulence frequency
f	Coriolis parameter
ρ_0	Base state density
U_g, V_g	Components of geostrophic wind in the x and y directions, respectively
z_i	Boundary layer height
z_{SL}	Surface layer height
Pr_t	Turbulent Prandtl number

fields can be calculated as:

$$\begin{aligned}
 \frac{\partial \bar{u}}{\partial t} &= -\frac{1}{\rho_0} \frac{\partial \rho_0 \overline{u'w'}}{\partial z} - f (V_g - \bar{v}), \\
 \frac{\partial \bar{v}}{\partial t} &= -\frac{1}{\rho_0} \frac{\partial \rho_0 \overline{v'w'}}{\partial z} + f (U_g - \bar{u}), \\
 \frac{\partial \bar{\theta}}{\partial t} &= -\frac{1}{\rho_0} \frac{\partial \rho_0 \overline{w'\theta'}}{\partial z},
 \end{aligned} \tag{14}$$

where f is the Coriolis parameter, ρ_0 is the base state density, and U_g and V_g are the components of geostrophic wind in the x and y directions, respectively. The detailed explanation and implementation of the model are available in Shin and Baik (2024). A list of symbols used in this study is provided in Table 2.

Table 3 List of the simulation cases and their setup for wind speed and surface fluxes, along with the time-averaged boundary layer height z_i , surface layer height z_{SL} , and friction velocity u_* during the last hour of the LSM simulations

Case	Wind (m s^{-1})	$(\overline{w'\theta'})_s$ (K m s^{-1})	$(\overline{w'q'})_s$ ($\text{g kg}^{-1} \text{m s}^{-1}$)	z_i (km)	z_{SL} (m)	u_* (m s^{-1})
W00	0	0.075	0.11	1.088	76	0.10
W02	2	0.075	0.11	1.088	76	0.21
W04	4	0.075	0.11	1.087	76	0.29
W06	6	0.075	0.11	1.084	78	0.37
W08	8	0.075	0.11	1.081	80	0.43
W10	10	0.075	0.11	1.080	82	0.50
W10_F50	10	0.0375	0.055	1.038	76	0.46
W10_F10	10	0.0075	0.011	0.989	112	0.41

2.3 Case Description and Model Setup

The test cases are idealized simulation cases of the convective boundary layer described in Maronga (2014). The potential temperature and specific humidity profiles are initialized with constant values of 298K for potential temperature and 12 g kg^{-1} for specific humidity up to a height of 950 m. Above this, a capping inversion layer depth of 250 m with lapse rates of 27 K km^{-1} for potential temperature and $13.8 \text{ g kg}^{-1} \text{ km}^{-1}$ for specific humidity is imposed. In the free atmosphere, the lapse rate is set to 7 K km^{-1} for potential temperature and zero for specific humidity. An aerodynamic roughness length is prescribed as 0.1 m. The test cases are forced by different geostrophic wind speeds and surface fluxes as specified in Table 3. The cases in Table 3 are listed in order of increasing stability or smaller contribution of buoyancy compared to shear. The surface momentum fluxes are diagnosed using the Businger–Dyer similarity functions and the horizontal wind speed of particles in the lowest model layer. More specifically, u_* is computed by averaging the local u_* derived from the horizontal wind speed of each particle in the lowest model layer, similar to how u_* is computed in LES. As the height of the lower model layer is sufficiently low, the stability correction is negligible in the calculation of the surface momentum fluxes (i.e. $-z/L \approx 0$).

The LSM simulations are conducted for all test cases, and the results are compared against the predictions of MOST. Each LSM simulation is run with a total particle count of $N_p = 1,000,000$, and both the model and particle integration time steps are set to $\Delta t = 0.5 \text{ s}$. The vertical grid configuration follows Maronga (2014), using 832 vertical grid points with a grid spacing of $\Delta z = 2 \text{ m}$. A small vertical grid size is necessary to resolve the ASL structure in the LSM simulations. The simulations are initialized with specified profiles of TKE and dissipation rate. The initial TKE is $0.4 \text{ m}^2 \text{ s}^{-2}$ at $z = 0 \text{ m}$ and decreases linearly to $0 \text{ m}^2 \text{ s}^{-2}$ at $z = 250 \text{ m}$. The initial dissipation rate is set by specifying the turbulence time scale (k/ϵ), where the turbulence time scale is 1 s at $z = 0 \text{ m}$ and increases linearly to 550 s at $z = 250 \text{ m}$, similar to Želi et al. (2020). Then, initial particle velocities are randomly perturbed according to the initial TKE profile.

Each simulation runs for 2 h and the final hour is used for the analysis. The simulation outputs including particle properties are saved each model time step. For the analysis of mean gradients and standard deviations (Sections 3.2, 3.3, and 3.4), statistics are averaged over 15-minute intervals, and the samples from heights ranging from 14 to 100 m (approximately the

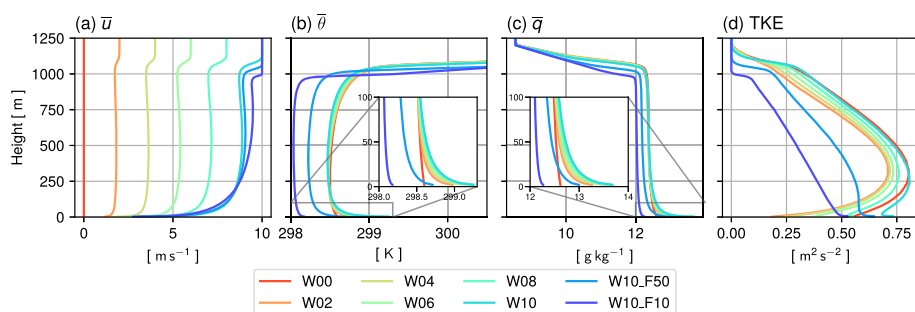


Fig. 1 Vertical profiles of **a** horizontal wind speed, **b** potential temperature, **c** specific humidity, and **d** turbulent kinetic energy from the LSM simulations

height of the ASL) are used. Other mean profiles are time averages, and turbulence PDFs are obtained using particle properties at every model time step during the analysis period.

3 Results

3.1 Simulated Boundary Layer Structure

Before examining the simulated statistics of the ASL, the characteristics of the simulated boundary layers are briefly discussed. Figure 1 shows the vertical profiles simulated by the LSM. The LSM simulates a well-mixed convective boundary layer structure with a pronounced entrainment zone similar to the LSM simulation in Shin and Baik (2024). Vertical profiles of horizontal wind speed, potential temperature, and specific humidity show strong gradients near the surface. Increasing geostrophic wind speed is related to deeper regions of strong wind gradients. For potential temperature and specific humidity profiles, the gradients near the surface gradually increase as geostrophic wind intensifies, but in W10_F50 and W10_F10, the gradients decrease due to reduced surface fluxes.

The test cases have strong capping inversion, so the boundary layer depth is only slightly deepened during the simulation period. In the simulations, the boundary layer depth is measured as the height at which the mean gradient of the potential temperature reaches its maximum. The simulated boundary layer depths are measured as 1.088–1.080 km for the cases from W00 to W10, 1.038 km for W10_F50, and 0.989 km for W10_F10 (Table 3). This result is similar to the LES results from Maronga (2014), where the boundary layer heights are measured as 1.08 km for the cases from W00 to W10, 1.04 km for W10_F50, and 1.00 km for W10_F10. A noticeable feature is that geostrophic wind speed has shown little impact on boundary layer height in our LSM simulations and also in the LESs. It is well known that vertical wind shear enhances the entrainment process at the convective boundary layer top (Moeng and Sullivan 1994; Kim et al. 2003), but the strong capping inversion in this setup might suppress the enhancement of entrainment. The top height of surface layer, z_{SL} , is measured as the height where $w'\theta'$ had decreased by 10% of its surface value, based on the typical definition of surface layer (Stull 1988). As the heat flux decreases linearly with height within the convective boundary layer, simulated z_{SL} is approximately 10% of boundary layer depth (Table 3). W10_F10 simulation shows exceptionally higher z_{SL} than other cases because the rate of heat flux decrease near the surface is relatively small in this case.

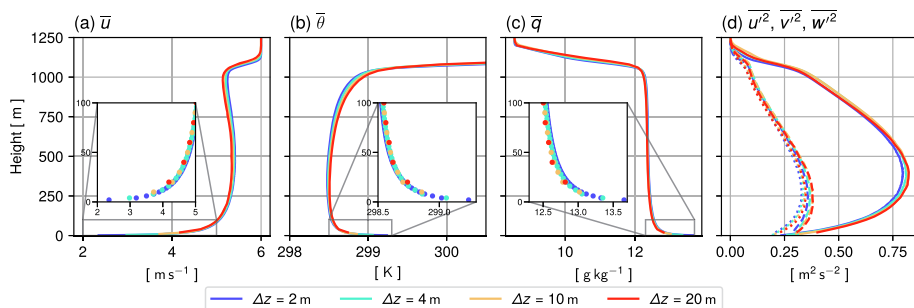


Fig. 2 Vertical profiles of **a** horizontal wind speed, **b** potential temperature, **c** specific humidity, and **d** variances of turbulent fluctuations of wind components from the LSM simulations with different vertical grid spacings ($\Delta z = \{20, 10, 4, 2\}$ m) for the W06 case. In the zoomed inset plots, points are plotted for each model layer. In **d**, the dashed, dotted, and solid lines represent the variances of the u -, v -, and w -wind fluctuations, respectively

As the geostrophic wind strengthens, TKE increases for most cases, with the exception of W00 (Fig. 1d). TKE is significantly reduced in lower surface flux cases, W10_F50 and W10_F10. The free-convection case W00 shows an exceptional result, producing higher TKE than the cases with weak geostrophic winds. This anomaly is likely due to an underestimation of dissipation. In W00, there is no dissipation production above the surface because the $C_{\epsilon 3}$ parameter is set to zero, resulting in a much lower dissipation rate than in cases with non-zero geostrophic winds. Another deficiency of W00 is an underestimation of friction velocity, u_* . Even when the mean wind is zero, the friction velocity can still be non-zero because large eddies can generate local shear near the surface (Schumann 1988; Akylas et al. 2003). Many boundary layer turbulence models address this issue by imposing a minimum threshold for friction velocity, typically within the range of 0.1 – 0.2 m s^{-1} . As described in Section 2.3, the friction velocity is computed by averaging the local u_* of each particle in the lowest model layer in the LSM, so the local shear effect is considered. However, the simulated u_* value of 0.1 m s^{-1} in W00 (Table 3) is considerably lower than the LES-simulated value of approximately 0.2 m s^{-1} (Maronga 2014), reflecting that the LSM underestimates near-surface horizontal velocity variance, as noted by Shin and Baik (2024). This result implies that the LSM underestimates the strength of large eddies in the convective boundary layer.

We also examine the resolution dependencies on simulated statistics. Figure 2 displays the simulation results of the W06 case with varying vertical grid spacing ($\Delta z = \{20, 10, 4, 2\}$ m). In these simulations, the number of particles and time steps are set to $N_p = \{1 \times 10^5, 2 \times 10^5, 5 \times 10^5, 1 \times 10^6\}$ and $\Delta t = \{5, 2.5, 1, 0.5\}$ s, respectively, to maintain consistent CFL numbers and particle counts per grid cell. The grid spacing dependency on the simulated profiles is small, with the profiles from different resolutions closely aligning. However, there is a systematic bias that simulations with coarser grid spacing tend to predict stronger turbulent mixing and deeper boundary layers.

3.2 Mean Gradient

Various similarity functions for the mean gradients for potential temperature and horizontal wind speed have been suggested in the Businger–Dyer form. In this study, we compare the model results with the similarity functions from Dyer (1974):

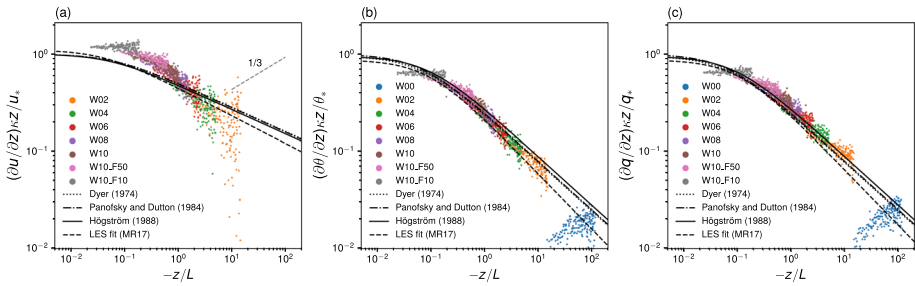


Fig. 3 Normalized mean gradients of **a** horizontal wind component, **b** potential temperature, and **c** specific humidity against the negative stability parameter $-z/L$. Scatter points represent samples from the LSM simulations, and the black lines are the MOST functions from various references (see text). The dashed line of slope 1/3 denotes the free-convection scaling

$$\Phi_m = 1.0 \left(1 - 15.2 \frac{z}{L}\right)^{-0.25}, \quad \Phi_h = 0.95 \left(1 - 15.2 \frac{z}{L}\right)^{-0.5}, \quad (15)$$

Panofsky and Dutton (1984):

$$\Phi_m = 1.0 \left(1 - 16.0 \frac{z}{L}\right)^{-0.25}, \quad \Phi_h = 1.0 \left(1 - 16.0 \frac{z}{L}\right)^{-0.5}, \quad (16)$$

Högström (1988):

$$\Phi_m = 1.0 \left(1 - 19.3 \frac{z}{L}\right)^{-0.25}, \quad \Phi_h = 0.95 \left(1 - 11.6 \frac{z}{L}\right)^{-0.5}, \quad (17)$$

and the LES fitting curves of Maronga and Reuder (2017):

$$\begin{aligned} \Phi_m &= 0.85 \left(0.4 - 9.5 \frac{z}{L}\right)^{-0.285}, \\ \Phi_h &= 1.1 \left(1.5 - 17.0 \frac{z}{L}\right)^{-0.57}, \quad \Phi_q = 1.1 \left(1.5 - 14.5 \frac{z}{L}\right)^{-0.57}. \end{aligned} \quad (18)$$

When compared with in-situ observations, as reviewed by Högström (1996), these similarity relations generally align with observed trends toward stability, although observations show some spread from the similarity relations. Under moderately unstable conditions, vertical turbulent mixing is stronger than in neutral and stable conditions, therefore the relations for Φ_m and Φ_h are relatively robust and the spread of observation is much smaller than in stable conditions (Foken 2006).

It is generally assumed that the similarity functions for temperature and humidity are identical ($\Phi_h = \Phi_q$). However, interactions between turnover eddies and profile deviations can cause variations in the similarity functions between different variables, as noted by Li et al. (2012b). In the proposed theory, the dissimilarity between Φ_m and Φ_h can be explained as the mixing length scale of temperature is smaller than that of horizontal velocity. The dissimilarity may occur between temperature and humidity as the correlation between the two variables is less than one (De Bruin et al. 1999; Li et al. 2012a).

Figure 3 displays the simulated gradients and similarity functions against $-z/L$. All gradients are normalized by the characteristic scales divided by κz . The data points from different LSM simulations converge onto a single curve, where normalized gradients decrease as $-z/L$ increases. The scatter of the data points is small, indicating that factors other than stability have little effect on the universality of the relationship. For both potential temperature and specific humidity, the simulation data closely align with the MOST predictions, following

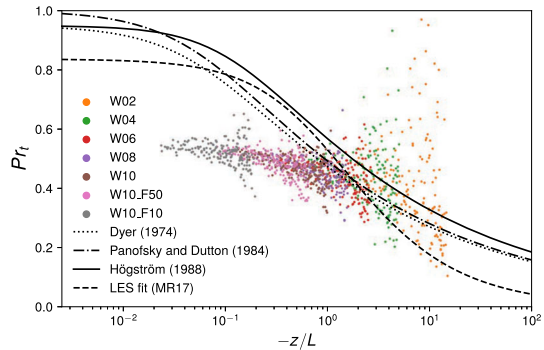
a slope of -0.5 (hereinafter, the slope means the slope along the stability parameter in a log-log space) under moderately unstable conditions (Fig. 3b and c). The results are also similar to those from the LES study (Maronga and Reuder 2017), but unlike the LES results, the scatters of W00 deviate from other cases, likely due to the reasons explained in Section 3.1. Additionally, the W00 scatter presents a distinct slope from other cases, indicating that the LSM underestimates scalar gradients close to the surface when wind shear is absent. Shin and Baik (2024) also reported an underestimation of scalar gradients in the simulation of shear-free convective boundary layer, attributing this underestimation to a significant underestimation of dissipation in the near-surface region.

Comparing the results for potential temperature and specific humidity, the normalized gradients for both variables are similar, though the gradient for specific humidity is slightly larger than that for potential temperature. Maronga and Reuder (2017) also reported that LES measured Φ_q is slightly larger than Φ_h . As noted above, such discrepancy can occur when the correlation between the two variables is less than one. In our LSM, the correlation between θ and q is mainly controlled by the scale and correlation of the noise terms in the SDEs. The noise terms of the SDEs for θ and q are assumed to be uncorrelated in the current implementation of the LSM. To explore how the correlation affects the similarity functions of the two variables, we conducted a sensitive simulation in which the random noises of the SDEs for θ and q are perfectly correlated ($dW_\theta = dW_q$). In this sensitivity simulation, the correlation between θ and q becomes one, and the normalized gradients of the two variables are found to be the same (not shown).

For horizontal wind speed, the normalized mean gradients of the LSM simulations exhibit a steeper slope than the curves predicted by MOST. The slope is close to -0.5 rather than the predicted value of -0.25 . According to the theory of Li et al. (2012b), the result suggests that the LSM may underestimate the integral length scale for horizontal wind speed. Figure 3a shows that the simulated magnitude of mean wind shear is larger than the MOST predictions in the cases with stronger wind shear. This implies that the vertical transport of horizontal momentum is underestimated in these cases, possibly because the horizontal velocity variances are underestimated in the LSM simulations. The LSM has an issue with inaccurately representing turbulence anisotropy near the surface, underestimating horizontal velocity variances (Shin and Baik 2024). To address this issue, the parameterizations for dissipation and pressure redistribution need to be improved to accurately represent the wall effect. Modeling studies suggest that the coefficients in pressure redistribution and dissipation parameterizations need to be modeled as functions of stability (van der Laan et al. 2017; Ayet et al. 2020).

The scatter in data points for horizontal wind speed is more pronounced than for potential temperature and specific humidity, with the scattering becoming more significant under increasingly unstable conditions. When $-z/L \gg 1$, buoyancy production dominates, reaching the free-convection limit. In the free-convection limit, the normalized mean gradients of horizontal wind speed are expected to follow a $1/3$ slope (Wyngaard et al. 1971). The data points of highly unstable cases tend to diverge, but they do not follow the expected $1/3$ slope. This suggests that the LSM may underestimate the strength of convection in the ASL, as further discussed in Section 3.6.

Fig. 4 Turbulent Prandtl number Pr_t against the negative stability parameter $-z/L$. Scatter points represent samples from the LSM simulations. The black lines represent Pr_t calculated using the similarity functions from various references (see text)



3.3 Turbulent Prandtl number

The turbulent Prandtl number Pr_t is defined as the ratio of the momentum eddy diffusivity to the heat transfer eddy diffusivity, and it can be expressed as:

$$Pr_t = \frac{u_*^2 / (\partial u_h / \partial z)}{(w'\theta')_s / (\partial \theta / \partial z)} = \frac{\Phi_h}{\Phi_m}, \quad (19)$$

within the MOST framework. The dissimilarity between Φ_h and Φ_m causes Pr_t to depend on the stability parameter, typically resulting in $Pr_t \leq 1$. Previous studies indicate that Pr_t in the neutral limit (denoted as $Pr_{t,neu}$) is generally less than one, where Businger et al. (1971) suggest 0.74, Kader and Yaglom (1972) suggest 0.72–0.87, and Högström (1996) suggests 0.95.

Figure 4 shows the turbulent Prandtl number Pr_t against $-z/L$. Along with the similarity function from Högström (1988), the analytic fitting function from the LES data is also plotted (Maronga and Reuder 2017):

$$Pr_t = 0.53 \left(0.49 - 0.51 \frac{z}{L} \right)^{-0.64}. \quad (20)$$

The LES data suggest $Pr_{t,neu} \approx 0.84$ in the neutral limit. Pr_t from the LSM simulations show some dependency on stability parameters, indicating that the LSM captures the increased efficiency of heat transfer relative to momentum transfer as instability increases. However, the dependency of Pr_t on stability is considerably smaller than observations. Simulated Pr_t is too small for weakly unstable cases and shows a large scatter for highly unstable cases. $Pr_{t,neu}$ in the LSM is estimated as about 0.55, which is considerably lower than observations.

How can the dependency of Pr_t on stability be improved in the LSM? Li et al. (2015) provide a theory for the ASL that explains $Pr_{t,neu}$ and the stability dependency of Pr_t , using their spectral budget model. According to the theory, these properties are controlled by the Rotta constants, isotropization constants, and other constants that define the turbulence spectrum, such as the Kolmogorov phenomenological constants. In our model, c_1 and $c_{1\phi}$ represent the Rotta constants, and c_2 and $c_{2\phi}$ represent the isotropization constants (assuming $c_{2\phi} = c_2$ for a simplified form of the SDEs, see Das and Durbin (2005)). Sensitivity simulations are conducted by modifying these constants, with the results shown in Fig. 5. In the sensitivity test where c_2 is adjusted from 0.6 to 0.4, the normalized gradients of horizontal wind are consistently decreased, leading to a better fit with the MOST prediction under near-neutral conditions (Fig. 5a). This results in the increase of $Pr_{t,neu}$ to about 0.8, and the dependency of Pr_t on stability is also improved (Fig. 5d). Adjusting the value of c_2 from

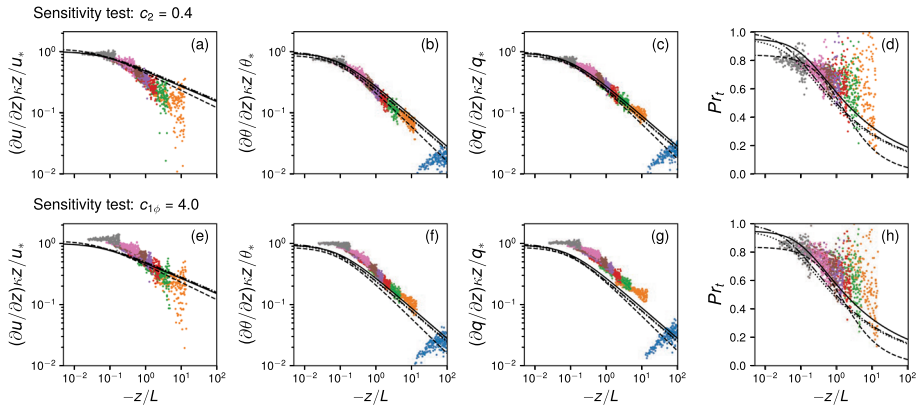


Fig. 5 Results of sensitivity tests with $c_2 = 0.4$ (first row) and $c_{1\phi} = 4.0$ (second row), showing the normalized mean gradients of **a,e** horizontal wind component, **b,f** potential temperature, **c,g** specific humidity, and **d,h** turbulent Prandtl number against the negative stability parameter $-z/L$. Colors and lines are as in Figs. 3 and 4

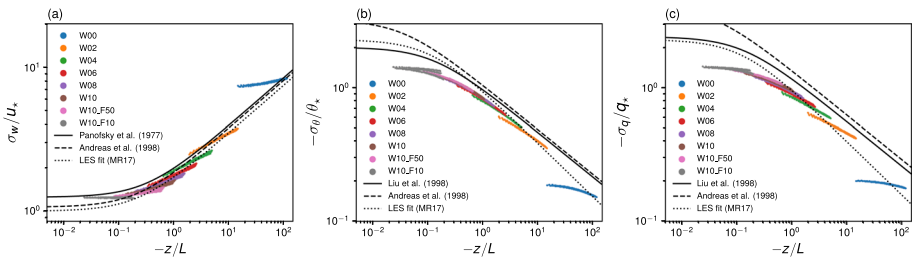


Fig. 6 Normalized standard deviations of **a** vertical velocity, **b** potential temperature, and **c** specific humidity against the negative stability parameter $-z/L$. Scatter points represent samples from the LSM simulations, and the black lines are the MOST functions from various references (see text)

0.6 to 0.4 reduces isotropization strength and increases turbulence anisotropy. The increased anisotropy enhances vertical mixing, which can reduce horizontal wind gradients. In the test where $c_{1\phi}$ (the Rotta constant for scalars) is adjusted from 2.5 to 4.0, the normalized gradients of horizontal wind remain unchanged, but those of θ and q consistently increase (Fig. 5f and g). Increasing $c_{1\phi}$ weakens the anisotropy of scalar fluctuations, thereby amplifying scalar gradients. The improvements in Pr_t are similar to those in the first sensitivity test. However, the slope of the normalized gradients of horizontal wind is not improved in these sensitivity simulations, so the simulated dependency of Pr_t on stability is still not fully satisfactory. As previously mentioned, accurate modeling of the wall effect is needed to improve the simulation of turbulence anisotropy and momentum transport.

3.4 Standard Deviation

Figure 6 shows the simulated normalized standard deviations of w , θ , and q . Previously proposed similarity functions for standard deviations in literature are notably deviated, so several functions are drawn for the comparison. These MOST functions are from Panofsky

et al. (1977):

$$\Phi_{\sigma_w} = 1.3 \left(1.0 - 3 \frac{z}{L}\right)^{1/3}, \quad (21)$$

Liu et al. (1998):

$$\Phi_{\sigma_\theta} = -2.0 \left(1 - 8 \frac{z}{L}\right)^{-1/3}, \quad \Phi_{\sigma_q} = -2.4 \left(1 - 8 \frac{z}{L}\right)^{-1/3}, \quad (22)$$

Andreas et al. (1998):

$$\begin{aligned} \Phi_{\sigma_w} &= 1.2 \left(0.7 - 3 \frac{z}{L}\right)^{1/3}, \\ \Phi_{\sigma_\theta} &= -3.2 \left(1 - 28.4 \frac{z}{L}\right)^{-1/3}, \quad \Phi_{\sigma_q} = -4.1 \left(1 - 28.4 \frac{z}{L}\right)^{-1/3}, \end{aligned} \quad (23)$$

and the LES fitting curves of Maronga and Reuder (2017):

$$\begin{aligned} \Phi_{\sigma_w} &= 1.0 \left(1.0 - 4.1 \frac{z}{L}\right)^{1/3}, \\ \Phi_{\sigma_\theta} &= -1.2 \left(0.2 - 1.7 \frac{z}{L}\right)^{-0.4}, \quad \Phi_{\sigma_q} = -1.2 \left(0.2 - 1.6 \frac{z}{L}\right)^{-0.4}. \end{aligned} \quad (24)$$

Note that the LES fitting curves for Φ_{σ_θ} and Φ_{σ_q} have different slopes compared to other MOST functions. Recent observational studies using datasets from various surface conditions indicate that near-surface scaling relations for standard deviations vary with turbulence anisotropy (Stiperski et al. 2019; Stiperski and Calaf 2023). However, the studies also demonstrated that under moderately unstable conditions ($0.1 < -z/L < 10$), Φ_{σ_w} and Φ_{σ_θ} exhibit a low dependency on turbulence anisotropy, and data from multiple stations show relatively small deviations from the MOST functions. Note that the standard deviations of horizontal velocities are not considered in this study, which are known to have a strong dependency on turbulence anisotropy.

The data points from the LSM simulations converge well into a single curve, with the slopes aligning closely with the MOST prediction ($1/3$ for vertical velocity and $-1/3$ for potential temperature and specific humidity). However, W00 exhibits exceptional behavior, showing a notable dependency on height, with its data points deviating from other cases. W00 shows such a deviation due to the underestimation of dissipation at the near-surface (therefore, σ_w is overpredicted), as explained in Section 3.2. For vertical velocity, the normalized σ_w simulated by the LSM closely follows MOST predictions. The LSM also reproduces a slight height dependency of normalized σ_w that is observed in the LES results (see Fig. 5c in Maronga and Reuder (2017)). For θ and q , the LSM simulates smaller normalized σ_θ and σ_q than predictions from Liu et al. (1998) and Andreas et al. (1998). The data points are more closely aligned with the LES fitting curves, but they still show smaller values under near-neutral conditions. Liu et al. (1998) and Andreas et al. (1998) found that normalized σ_q is slightly greater than normalized σ_θ . LSM also simulates about 10% larger normalized σ_q compared to normalized σ_θ on average.

3.5 Turbulent Kinetic Energy Budget

The budget equation for TKE is:

$$\frac{Dk}{Dt} = T^t + T^p + \mathcal{P} + \mathcal{G} - \epsilon, \quad (25)$$

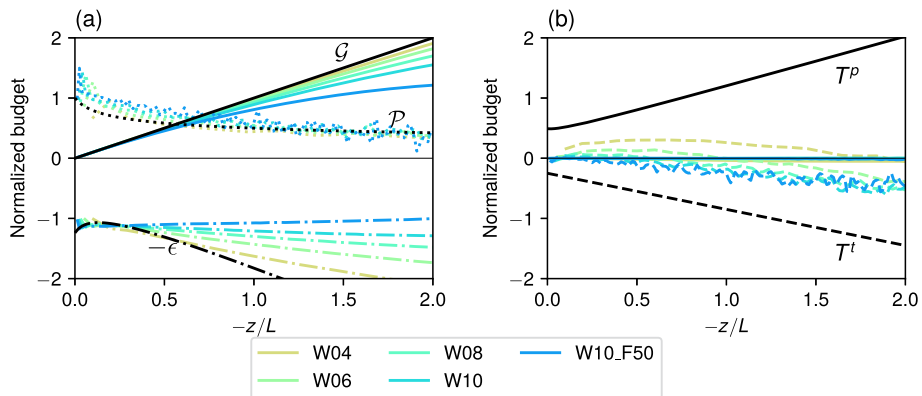


Fig. 7 Components of the turbulence energy budget as a function of $-z/L$, showing **a** buoyancy production \mathcal{G} (solid), shear production \mathcal{P} (dotted), dissipation ϵ (dash-dotted), **b** turbulent transport T^t (dashed), and pressure transport T^p (solid), all normalized by $\kappa z / u_*^3$. The predictions from MOST are colored black, and the budgets from the LSM are colored as the legend

where T^t is the turbulent transport and T^p is the pressure transport. In the ASL, the production terms can be expressed as:

$$\mathcal{P} \equiv -\overline{u'_i u'_j} \frac{\partial U_i}{\partial x_j} = \frac{u_*^3}{\kappa z} \Phi_m, \quad (26)$$

$$\mathcal{G} \equiv \frac{g}{\theta_{v0}} \overline{w' \theta'_v} = -\frac{u_*^3}{\kappa z} \zeta, \quad (27)$$

where $\zeta = z/L$. While some similarity functions for transport and dissipation terms have been proposed (McNaughton 2006; Kooijmans and Hartogensis 2016), we utilize the relation proposed by Högström (1990):

$$T^t = -\frac{u_*^3}{\kappa z} \times \begin{cases} -0.6\zeta + 0.25 & \zeta < 0 \\ 0.25 & \zeta \geq 0 \end{cases}, \quad (28)$$

$$T^p = -\frac{u_*^3}{\kappa z} \times \begin{cases} -0.25 + 0.84\zeta - 0.24(1 - 19\zeta)^{-1/4} & \zeta < 0 \\ -0.49 - 0.9\zeta & \zeta \geq 0 \end{cases}, \quad (29)$$

$$\epsilon = \frac{u_*^3}{\kappa z} \times \begin{cases} 1.24[(1 - 19\zeta)^{-1/4} - \zeta] & \zeta < 0 \\ 1.24 + 4.7\zeta & \zeta \geq 0 \end{cases}. \quad (30)$$

Figure 7 shows the normalized budget terms from the LSM simulations and the MOST relations. Simulation cases in which $-L$ is too small or large (W00, W02, and W10_F10) are excluded from the figure. When $-z/L \approx 0$, the buoyancy production is negligible compared to other terms, and the shear production is approximately balanced by dissipation. As height increases, the shear production decreases rapidly, while the contribution of buoyancy production becomes more significant. As shown in Fig. 7a, the buoyancy and shear productions simulated by the LSM are in line with the MOST predictions, with some deviations. The simulated buoyancy productions become lower than the MOST prediction as height increases, and this is an expected behavior because buoyancy fluxes linearly decrease within the boundary layer. The LSM overestimates shear production for $-z/L < 1$, indicating the overestimation of Φ_m which we already seen in Fig. 3a.

Relatively large errors appear in the dissipation and transport terms. At $-z/L \approx 0$, the simulated normalized dissipation is close to the MOST predicted value of 1, but the LSM increasingly underestimates the dissipation as height increases. The error is more pronounced in less unstable conditions. Regarding the transport terms, the LSM simulates almost negligible pressure transport compared to the MOST predictions, leading to considerable errors in total TKE transport within the ASL. This might be problematic in higher-order closure models too, as the pressure transport term is generally neglected or jointly modeled with turbulent transport. Although pressure transport is generally less significant than turbulent transport in the boundary layer (typically less than 20%), its contribution to the unstable ASL is substantial, even exceeding that of turbulent transport. In addition, pressure transport is an important mechanism that enhances thermal convection and increases TKE in the unstable ASL (Lin 2000). Therefore, accurate modeling of pressure transport is crucial for realistically simulating vertical turbulence structure within the unstable ASL.

The LSM also underestimates the magnitude of turbulent transports compared to the MOST prediction (Fig. 7b). The simulated turbulent transports even exhibit an opposite sign in W04 and W06. Since turbulent transport in the LSM is calculated exactly rather than parameterized, these errors in turbulent transport might originate from the inaccuracy of turbulence PDF. Generally, the turbulent transport term acts to balance other terms, so improving the modeling of dissipation and pressure transport would also lead to more accurate turbulent transport predictions. As will be discussed in the next subsection, incorporating information on turbulence PDF is important for improving the modeling of dissipation and pressure transport.

3.6 Probability Density Function

In many practical applications, the turbulence PDF within the ASL is often assumed to be Gaussian. However, inhomogeneous turbulence frequently exhibits non-Gaussian characteristics, particularly under unstable conditions (Liu et al. 2011). The joint PDFs simulated by the LSM reveal the detailed shape of the distribution within the ASL, which cannot be simulated by higher-order closure models (Fig. 8). The joint PDF of w and θ (or q) shows a curved shape, where the distribution of θ (or q) is positively skewed in the positive vertical velocity region. The skewness increases with increasing height, indicating the development of thermal convection as height increases. The joint PDF of θ and q shows a diagonally skewed shape because both variables are positively skewed.

In the MOST framework, the correlation between vertical velocity and potential temperature (or specific humidity) can be calculated as:

$$\begin{aligned} r_{w\theta} &= \left(\overline{w'\theta'} \right)_s / (\sigma_w \sigma_\theta) = -1 / (\Phi_{\sigma_w} \Phi_{\sigma_\theta}), \\ r_{wq} &= \left(\overline{w'q'} \right)_s / (\sigma_w \sigma_q) = -1 / (\Phi_{\sigma_w} \Phi_{\sigma_q}), \end{aligned} \quad (31)$$

assuming that the vertical fluxes are constant within the ASL. However, the correlation between θ and q , denoted as $r_{\theta q}$, can not be determined using this approach because the covariance between θ and q is unknown. Liu et al. (1998) determined $r_{\theta q}$ using the following relationship:

$$|r_{\theta q}| = |r_{wq}| / |r_{w\theta}| = |\Phi_{\sigma_\theta} / \Phi_{\sigma_q}| \approx 0.83, \quad (32)$$

based on the observations that $r_{\theta q}$ is close to the constant value of 0.83.

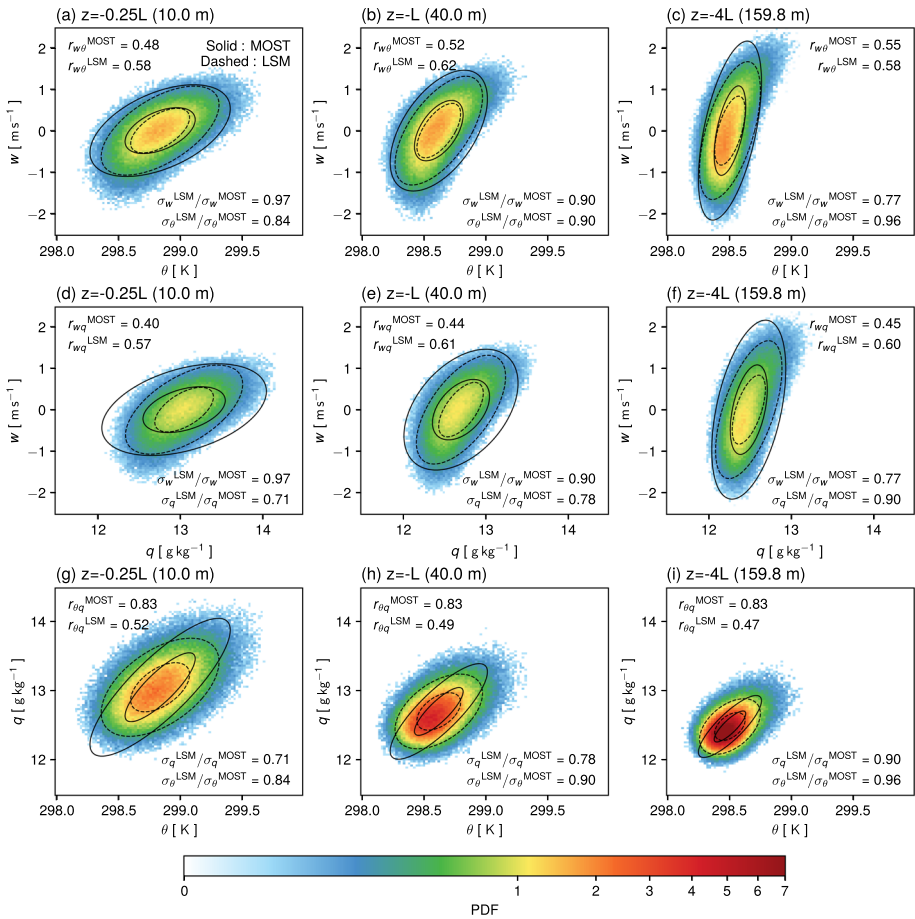


Fig. 8 Joint PDFs for (first row) θ and w , (second row) q and w , and (third row) θ and q are shown for the LSM simulation of the W06 case at three different heights: (first column) $z = -0.25L$, (second column) $z = -L$, and (third column) $z = -4L$. The black solid and dashed ellipses show one σ range of the joint PDF derived from the MOST and LSM, respectively. The correlation coefficients (r) between the two variables are displayed at the top of each panel, and the ratios of standard deviations from the MOST to LSM are displayed at the bottom of each panel. Here, the MOST functions of Liu et al. (1998) are used for the comparison. The unit of each PDF is the reciprocal of the product of the units of the two variables represented on the x and y axes

In Fig. 8, the simulated joint PDFs are compared with MOST predictions using bivariate Gaussians determined from the predicted standard deviations and correlations. As height increases, the standard deviations of vertical velocity increase and the standard deviations of potential temperature and specific humidity decrease. The LSM reproduces this dependency on stability well, as shown in Fig. 6. Note that $r_{w\theta}$ and r_{wq} exhibit small variations along stability as σ_w increases with the slope of $1/3$ and σ_w and σ_q decrease with the slope of $-1/3$. Compared to the MOST functions of Liu et al. (1998), the LSM simulates smaller values for σ_θ and σ_q , resulting in larger values for $r_{w\theta}$ and r_{wq} than those predicted by MOST. In the case of $r_{\theta q}$, the LSM produces smaller values of $r_{\theta q}$ compared to the MOST-predicted value

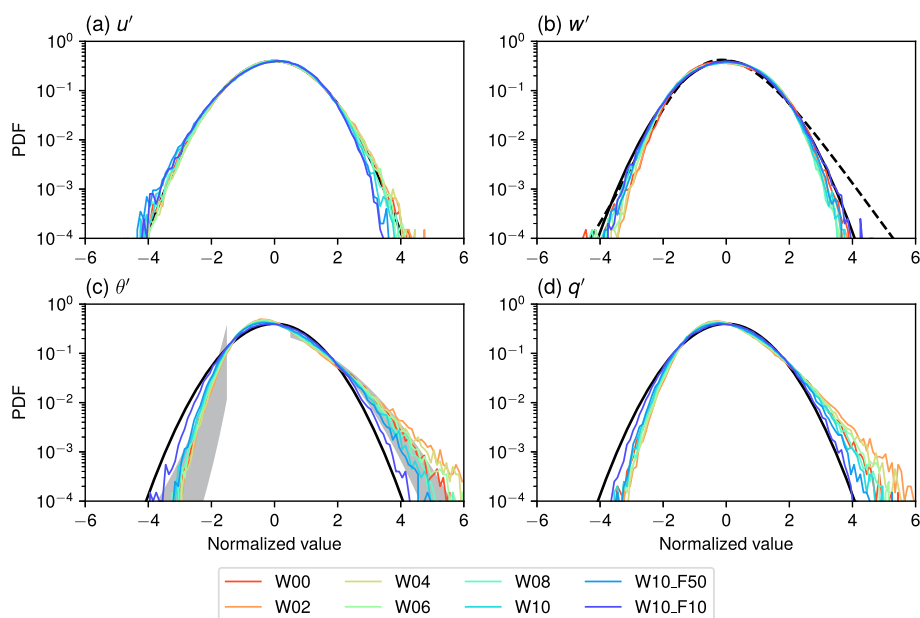


Fig. 9 Probability density functions of normalized **a** longitudinal velocity fluctuations, **b** vertical velocity fluctuations, **c** potential temperature fluctuations, and **d** specific humidity fluctuations at a height of 50 m, simulated by the LSM. The solid lines are Gaussian distributions, and the dashed line in **b** is the fitted analytic function for the distribution of vertical velocity fluctuation from Liu et al. (2011). The gray shades in **c** are the range of fitted tail distributions from Liu et al. (2011). See text for more details

of 0.83. In the sensitivity simulation where the noise terms are perfectly correlated (which is explained in Section 3.2), the correlation between the two variables becomes unity.

The turbulence PDFs simulated by the LSM are evaluated based on the study of Liu et al. (2011), which investigates PDFs in the unstable ASL in the framework of similarity theory (Fig. 9). Early studies on PDFs in the unstable ASL found that the PDF of horizontal velocity is nearly Gaussian, while the PDFs of vertical velocity and potential temperature are non-Gaussian (Chu et al. 1996; Anfossi et al. 1997). Liu et al. (2011) introduced a non-Gaussian fitting PDF for vertical velocity as a truncated stable distribution (dashed line in Fig. 9b). Measurements under various stability conditions collapse to a single truncated stable distribution line. The PDF of potential temperature is more complicated, and Liu et al. (2011) suggests that the left tails of the PDF approximately follow a power-law distribution and the right tails follow Gaussian. The PDF of potential temperature varies significantly with stability, and the range of tail distributions for $-z/L$ values from 0 to 2 is depicted as gray-shaded areas in Fig. 9c.

The PDFs of u' simulated by the LSM follow Gaussian distribution, consistent with what other observational studies have shown. In the case of w' , the LSM struggles to capture the non-Gaussian characteristics, instead producing distributions close to Gaussian. The probability of high vertical velocities ($w' > 2.5\sigma_w$) is considerably underestimated compared to the fitting curve of Liu et al. (2011). The skewness of the vertical velocity PDF becomes pronounced when $-z/L > 7$, which corresponds to heights above the ASL in weakly unstable cases (not shown). The LSM still simulates a highly skewed w' distribution in the lower part of the convective boundary layer (Shin and Baik 2024). The underestimation of the high

vertical velocity frequency in the unstable ASL indicates that the initial development of thermal convection is not well represented in the LSM. This means that improvements are needed in the representation of physical processes that generate convective updrafts with high vertical velocities near the surface.

The simulated PDFs of θ' capture the non-Gaussian characteristics, with shapes similar to those observed by Liu et al. (1998) (Fig. 9c). Consistent with the observation, high-temperature samples are more frequent in highly unstable cases. The right tails of the simulated distributions match well with the fitted tail distribution from Liu et al. (1998) in both shape and range. However, the simulated left tails exhibit a higher probability density than the fitted distributions. The simulated PDFs of q' closely resemble those of θ' , and this similarity between the PDFs of θ' and q' is also expected in real observations.

The underestimation of high vertical velocity probability contributes to the underestimation of turbulent transport, which consequently impacts the vertical structure of the unstable ASL. Furthermore, in a simulation of a moist convection case, convective clouds can be underpredicted due to weak initiation. We suspect that the reasons for this deficiency are as follows. First, the dissipation rate is homogeneous at each level in the LSM. However, in reality, dissipation is highly inhomogeneous and correlated with turbulent velocities in inhomogeneous turbulence (Van Slooten et al. 1998; Pope 2000). Strong updrafts can develop when the local dissipation rate is low, as these updrafts have a longer time scale for mixing. Second, the pressure transport parameterization used in the LSM does not perform well in the ASL. The pressure transport parameterization in Equation 10, proposed by Van Slooten et al. (1998), is designed for free shear flow, but its effectiveness is not guaranteed for stratified and/or wall-bounded turbulence. This parameterization accelerates high-energy particles in the direction of the TKE gradient, but the TKE gradient in the ASL is too weak for it to function effectively.

4 Summary and Conclusions

In this study, we evaluated the performance of a recently developed Lagrangian stochastic model (LSM) for simulating the turbulent structure of the unstable ASL. The LSM is capable of simulating full PDF of turbulence and exact calculation of turbulent transport, thus evaluating the LSM against MOST provides insights on how the Reynolds stress modeling can be improved for simulating stratified boundary layer turbulence. The LSM was tested against the MOST predictions for mean gradients, standard deviations, turbulent Prandtl number, TKE budgets, and turbulence PDFs.

Our analysis revealed that the LSM is capable of reproducing many key aspects of ASL structure and turbulence characteristics. The simulated mean gradients of potential temperature and specific humidity align closely with MOST predictions, and the dependency of gradients against stability follows the expected trends under moderately unstable conditions. However, the LSM tends to underestimate the dependency of gradients of horizontal wind speed against stability. This issue may stem from several model deficiencies, particularly the overestimation of the mixing length scale for horizontal velocity and the lack of stability dependency in dissipation and pressure redistribution.

The turbulent Prandtl number (Pr_t) simulated by the LSM showed some dependency on stability, indicating that the model is capable of capturing the increased efficiency of heat transfer relative to momentum transfer under unstable conditions. However, the Pr_t dependency on stability is underestimated than MOST predictions, and Pr_t at the neutral

limit is also lower than observed values. Adjusting the Rotta and isotropization constants can correct Pr_t at the neutral limit to match observed values, but further refinement in the modeling of dissipation and pressure redistribution is needed to achieve realistic dependency of Pr_t against stability. For the standard deviations of w , θ , and q , the LSM simulates a realistic stability dependency, though the standard deviations of θ and q are slightly underestimated compared to MOST predictions.

The LSM realistically simulates the Gaussian distribution of horizontal wind fluctuations and the non-Gaussian distribution of potential temperature fluctuations, along with its dependency on stability. However, the model exhibits limitations in capturing the non-Gaussian characteristics of vertical velocity fluctuations, where it underestimates the probability of high vertical velocities. This suggests that the initiation of thermal convection is less pronounced in the model. Consequently, this underestimation leads to an overall underprediction of turbulent transport. In real scenarios, local pressure transport plays a significant role in developing convection in the unstable ASL. However, the LSM simulates pressure transport that is too weak, as indicated by the TKE budget analysis.

In summary, to simulate turbulence statistics and mean profiles consistent with MOST, improvements are needed in the parameterizations for dissipation, pressure redistribution, and pressure transport to ensure that they have the correct stability dependency. While these improvements present significant challenges, the LSM offers a more flexible modeling framework compared to other turbulence closure models, as it can utilize the full turbulence PDF for parameterization. For example, the LSM of Pope (1991) simulates joint PDF of velocity and dissipation by formulating velocity SDE using the dissipation of each particle, so the inhomogeneity of dissipation is considered in the model. Large-scale coherent motion can be represented in this model, so a similar approach can be used in our model to improve the simulation of thermal convection. Future work will focus on refining these parameterizations to more accurately represent the non-Gaussian characteristics of turbulence, which are essential for simulating the ASL and its interactions with the upper atmospheric boundary layer.

Additionally, future studies should conduct more rigorous evaluations of the LSM. Comparing simulated statistics between the LSM and turbulence closure models will clarify the impact of the exact turbulent transport calculation in the LSM. While this study focuses on idealized, steady-state turbulence statistics, validation with real-world cases and in-situ observations will be valuable for assessing the model's performance in capturing transient statistics. This study assumes the ASL over a flat, horizontally homogeneous surface under moderately unstable conditions where the assumptions of MOST are generally valid. However, real-world observations involve surface heterogeneity and large coherent motions across a broad range of stability conditions, where traditional MOST assumptions fail to hold. In particular, observations on horizontal momentum variances under unstable stratification and vertical velocity and temperature variances under stable stratification cannot be represented by simple functions of stability. Future research will conduct a comprehensive evaluation of the LSM using multiple observational datasets to assess its ability to reproduce these complex behaviors under a full range of stability regimes.

Acknowledgements The authors are grateful to three anonymous reviewers for providing valuable comments on this work.

Funding Open Access funding enabled and organized by Seoul National University. This work was funded by the Korea Meteorological Administration Research and Development Program under Grant RS-2024-00404042. This work was also supported by the National Research Foundation of Korea (NRF) grant funded

by the Korea government (MSIT) (No. RS-2023-00214037) and the Pukyong National University Research Fund in 2023 (202315510001).

Open Access This article is licensed under a Creative Commons Attribution 4.0 International License, which permits use, sharing, adaptation, distribution and reproduction in any medium or format, as long as you give appropriate credit to the original author(s) and the source, provide a link to the Creative Commons licence, and indicate if changes were made. The images or other third party material in this article are included in the article's Creative Commons licence, unless indicated otherwise in a credit line to the material. If material is not included in the article's Creative Commons licence and your intended use is not permitted by statutory regulation or exceeds the permitted use, you will need to obtain permission directly from the copyright holder. To view a copy of this licence, visit <http://creativecommons.org/licenses/by/4.0/>.

References

- Akylas E, Tsakos Y, Tombrou M, Lalas DP (2003) Considerations on minimum friction velocity. *Q J R Meteorol Soc* 129(591):1929–1943
- Alinot C, Masson C (2005) k - ϵ model for the atmospheric boundary layer under various thermal stratifications. *J Solar Energy Eng* 127(4):438–443
- Andreas EL, Hill RJ, Gosz JR, Moore DI, Otto WD, Sarma AD (1998) Statistics of surface-layer turbulence over terrain with metre-scale heterogeneity. *Boundary-Layer Meteorol* 86(3):379–408
- Anfossi D, Ferrero E, Sacchetti D, Castelli ST (1997) Comparison among empirical probability density functions of the vertical velocity in the surface layer based on higher order correlations. *Boundary-Layer Meteorol* 82(2):193–218
- Apsley DD, Castro IP (1997) A limited-length-scale k - ϵ model for the neutral and stably-stratified atmospheric boundary layer. *Boundary-Layer Meteorol* 83:75–98
- Ayet A, Katul GG, Bragg AD, Redelsperger JL (2020) Scalewise return to isotropy in stratified boundary layer flows. *J Geophys Res Atmos* 125(16):e2020JD032732
- Bogenschutz PA, Gettelman A, Morrison H, Larson VE, Craig C, Schanen DP (2013) Higher-order turbulence closure and its impact on climate simulations in the community atmosphere model. *J Clim* 26(23):9655–9676
- Businger JA, Wyngaard JC, Izumi Y, Bradley EF (1971) Flux-profile relationships in the atmospheric surface layer. *J Atmos Sci* 28(2):181–189
- Chu CR, Parlange MB, Katul GG, Albertson JD (1996) Probability density functions of turbulent velocity and temperature in the atmospheric surface layer. *Water Resour Res* 32(6):1681–1688
- Das SK, Durbin PA (2005) A Lagrangian stochastic model for dispersion in stratified turbulence. *Phys Fluids* 17(2):025109
- De Bruin HAR, Van Den Hurk BJJM, Kroon LJM (1999) On the temperature-humidity correlation and similarity. *Boundary-Layer Meteorol* 93:453–468
- Dyer A (1974) A review of flux-profile relationships. *Boundary-Layer Meteorol* 7:363–372
- Foken T (2006) 50 years of the Monin–Obukhov similarity theory. *Boundary-Layer Meteorol* 119:431–447
- Golaz JC, Larson VE, Cotton WR (2002) A pdf-based model for boundary layer clouds. Part I: method and model description. *J Atmos Sci* 59(24):3540–3551
- Högström U (1988) Non-dimensional wind and temperature profiles in the atmospheric surface layer: a re-evaluation. *Boundary-Layer Meteorol* 42:55–78
- Högström U (1990) Analysis of turbulence structure in the surface layer with a modified similarity formulation for near neutral conditions. *J Atmos Sci* 47(16):1949–1972
- Högström U (1996) Review of some basic characteristics of the atmospheric surface layer. *Boundary-Layer Meteorol* 78:215–246
- Jenny P, Pope SB, Muradoglu M, Caughey DA (2001) A hybrid algorithm for the joint PDF equation of turbulent reactive flows. *J Comput Phys* 166(2):218–252
- Kader BA, Yaglom AM (1972) Heat and mass transfer laws for fully turbulent wall flows. *Int J Heat Mass Transf* 15(12):2329–2351
- Kim SW, Park SU, Moeng CH (2003) Entrainment processes in the convective boundary layer with varying wind shear. *Boundary-Layer Meteorol* 108:221–245
- Kooijmans LMJ, Hartogensis OK (2016) Surface-layer similarity functions for dissipation rate and structure parameters of temperature and humidity based on eleven field experiments. *Boundary-Layer Meteorol* 160:501–527

- Li D, Bou-Zeid E, De Bruin HAR (2012a) Monin–Obukhov similarity functions for the structure parameters of temperature and humidity. *Boundary-Layer Meteorol* 145:45–67
- Li D, Katul GG, Bou-Zeid E (2012b) Mean velocity and temperature profiles in a sheared diabatic turbulent boundary layer. *Phys Fluids* 24(10)
- Li D, Katul GG, Zilitinkevich SS (2015) Revisiting the turbulent Prandtl number in an idealized atmospheric surface layer. *J Atmos Sci* 72(6):2394–2410
- Lin CL (2000) Local pressure-transport structure in a convective atmospheric boundary layer. *Phys Fluids* 12(5):1112–1128
- Liu L, Hu F, Cheng XL (2011) Probability density functions of turbulent velocity and temperature fluctuations in the unstable atmospheric surface layer. *J Geophys Res Atmos* 116(D12)
- Liu X, Tsukamoto O, Oikawa T, Ohtaki E (1998) A study of correlations of scalar quantities in the atmospheric surface layer. *Boundary-Layer Meteorol* 87(3):499–508
- Maronga B (2014) Monin–Obukhov similarity functions for the structure parameters of temperature and humidity in the unstable surface layer: results from high-resolution large-eddy simulations. *J Atmos Sci* 71(2):716–733
- Maronga B, Reuder J (2017) On the formulation and universality of Monin–Obukhov similarity functions for mean gradients and standard deviations in the unstable surface layer: results from surface-layer-resolving large-eddy simulations. *J Atmos Sci* 74(4):989–1010
- McNaughton KG (2006) On the kinetic energy budget of the unstable atmospheric surface layer. *Boundary-Layer Meteorol* 118:83–107
- Moeng CH, Sullivan PP (1994) A comparison of shear- and buoyancy-driven planetary boundary layer flows. *J Atmos Sci* 51(7):999–1022
- Monin AS, Obukhov AM (1954) Basic laws of turbulent mixing in the surface layer of the atmosphere. *Contrib Geophys Inst Slovak Acad Sci* 24(151):163–187
- Muradoglu M, Pope SB, Caughey DA (2001) The hybrid method for the PDF equations of turbulent reactive flows: consistency conditions and correction algorithms. *J Comput Phys* 172(2):841–878
- Panofsky HA, Dutton JA (1984) *Atmospheric turbulence: models and methods for engineering applications*. Wiley, New York
- Panofsky HA, Tennekes H, Lenschow DH, Wyngaard J (1977) The characteristics of turbulent velocity components in the surface layer under convective conditions. *Boundary-Layer Meteorol* 11(3):355–361
- Pope S (1991) Application of the velocity-dissipation probability density function model to inhomogeneous turbulent flows. *Phys Fluids A* 3(8):1947–1957
- Pope SB (1995) Particle method for turbulent flows: integration of stochastic model equations. *J Comput Phys* 117(2):332–349
- Pope SB (2000) *Turbulent flows*. Cambridge University Press, Cambridge
- Schumann U (1988) Minimum friction velocity and heat transfer in the rough surface layer of a convective boundary layer. *Boundary-Layer Meteorol* 44(4):311–326
- Shin J, Baik JJ (2024) Lagrangian stochastic modeling of stratified atmospheric boundary layer. *Boundary-Layer Meteorol* 190(4):1–27
- Shin J, Park S (2020) A stochastic unified convection scheme (UNICON). Part I: Formulation and single-column simulation for shallow convection. *J Atmos Sci* 77(2):583–610
- Sørensen NN (1995) General purpose flow solver applied to flow over hills. PhD thesis, Technical University of Denmark, Roskilde, Denmark
- Stiperski I, Calaf M (2023) Generalizing Monin–Obukhov similarity theory (1954) for complex atmospheric turbulence. *Phys Rev Lett* 130(12):124001
- Stiperski I, Calaf M, Rotach MW (2019) Scaling, anisotropy, and complexity in near-surface atmospheric turbulence. *J Geophys Res Atmos* 124(3):1428–1448
- Stull RB (1988) *An introduction to boundary layer meteorology*. Kluwer Academic Publishers, Dordrecht
- Sumner J, Masson C (2012) The Apsley and Castro limited-length-scale k - ϵ model revisited for improved performance in the atmospheric surface layer. *Boundary-Layer Meteorol* 144(2):199–215
- Suselj K, Kurowski MJ, Teixeira J (2019) A unified eddy-diffusivity/mass-flux approach for modeling atmospheric convection. *J Atmos Sci* 76(8):2505–2537
- van der Laan MP, Kelly MC, Sørensen NN (2017) A new k - ϵ model consistent with Monin–Obukhov similarity theory. *Wind Energy* 20(3):479–489
- Van Slooten PR, Jayesh Pope SB (1998) Advances in PDF modeling for inhomogeneous turbulent flows. *Phys Fluids* 10(1):246–265
- Wilson J (2008) Monin–Obukhov functions for standard deviations of velocity. *Boundary-Layer Meteorol* 129(3):353–369
- Wyngaard J, Coté O, Izumi Y (1971) Local free convection, similarity, and the budgets of shear stress and heat flux. *J Atmos Sci* 28(7):1171–1182

- Želi V, Brethouwer G, Wallin S, Johansson AV (2019) Consistent boundary-condition treatment for computation of the atmospheric boundary layer using the explicit algebraic Reynolds-stress model. *Boundary-Layer Meteorol* 171(1):53–77
- Želi V, Brethouwer G, Wallin S, Johansson AV (2020) Modelling of stably stratified atmospheric boundary layers with varying stratifications. *Boundary-Layer Meteorol* 176(2):229–249
- Zeng X, Wang Y (2020) A k - ε turbulence model for the convective atmosphere. *J Atmos Sci* 77(11):3891–3906

Publisher's Note Springer Nature remains neutral with regard to jurisdictional claims in published maps and institutional affiliations.